Nonlinear characterization of robust multimaterial chalcogenide nanotapers for infrared supercontinuum generation

Soroush Shabahang, Guangming Tao, Michael P. Marquez, Honghua Hu, Trenton R. Ensley, Peter J. Delfyett, and Ayman F. Abouraddy*

CREOL, The College of Optics & Photonics, University of Central Florida, Orlando, Florida 32816, USA
**Corresponding author: raddy@creol.ucf.edu*

Received October 3, 2013; accepted November 19, 2013;
posted December 24, 2013 (Doc. ID 198877); published February 10, 2014

We present the results of an investigation of the nonlinear characteristics of a new class of robust, multimaterial, all-solid chalcogenide nanotapers prepared from high-index-contrast chalcogenide fibers. The fiber is drawn from a preform produced by multimaterial coextrusion and consists of chalcogenide core and cladding (which dictate the optical properties) and a built-in thermally compatible polymer jacket that provides mechanical stability to the fibers and nanotapers. We measure the nonlinear refractive indices both in the bulk chalcogenide glasses using the Z-scan method and directly in the nanotapers from spectral broadening resulting from self-phase modulation using both picosecond and femtosecond pulses. Such robust nanotapers offer many opportunities for dispersion engineering to optimize nonlinear optical fiber applications such as infrared supercontinuum generation. Low-power femtosecond pulses (~100 W peak power, corresponding to ~40 pJ energy per pulse) centered at 1.55 μm wavelength launched into the nanotapers generated a supercontinuum extending over a full spectral octave, 1–2 μm. A computational model that takes into account the relevant linear and nonlinear optical parameters provides simulations that are in good agreement with the supercontinuum measurements.

OCIS codes: (190.4370) Nonlinear optics, fibers; (320.6629) Supercontinuum generation.
http://dx.doi.org/10.1364/JOSAB.31.000450

1. INTRODUCTION

Chalcogenide glasses (ChGs) stand out as the only family of optical materials that are transparent across both the near- and mid-infrared (MIR) and that also can be thermally drawn continuously and stably into extended optical fibers [1,2]. Crucially, ChGs exhibit higher optical nonlinearities than rival infrared glasses. For example, the ChG As_2Se_3 has approximately 1 order of magnitude higher nonlinear refractive index n_2 compared to tellurite glasses, 2 orders of magnitude higher than fluoride (ZBLAN) glasses, and 3 orders of magnitude higher than silica glass [3], while maintaining a wider transparency window than tellurite, fluoride, or silicate glasses. A wide range of applications for ChG fibers can benefit from this combination of useful optical characteristics ranging from high-speed optical communication that requires ultrafast all-optical processing and switching [4–10] to MIR supercontinuum generation (SCG) [11,12] for spectroscopy and countermeasures (complementing SCG in tellurite [13,14] and fluoride [15,16] fibers).

The use of fibers in nonlinear optical applications offers obvious advantages in increasing the nonlinear interaction length, obviating the need for optical alignment, in addition to mechanical stability, which are critical advantages in harsh or unstable environments. Nevertheless, well-known difficulties in processing ChGs hamper their utilization in the fiber form factor. Indeed, current fabrication approaches face challenges in controlling the core diameter, the core-to-cladding diameter ratio and index contrast, and the fiber outer diameter. Despite the decades-long development of ChG fibers [17], harnessing their high optical nonlinearity has been curtailed by their poor power-handling capabilities [18,19] and large normal group velocity dispersion (GVD) [20,21]. To overcome these obstacles in ChG fibers, novel approaches are required, particularly to achieve broadband SCG. For example, cascaded Raman frequency shifting [12,22,23] has been used in conjunction with long pump pulses (tens of picoseconds to nanoseconds) to produce spectral broadening via stimulated Raman scattering. While the long pump pulses help reduce the deleterious impact of large GVD, the generated supercontinua are expected to be incoherent [24].

To date, three strategies have been explored to overcome the high ChG material GVD by balancing it with counteracting waveguide GVD. The first strategy relies on high-index-contrast composite fibers, such as ChG/silica step-index fibers [25], ChG/polymethyl methacrylate (PMMA) hybrid microwires [26,27], and ChG-core/tellurite-cladding microstructured fibers [28]. The new material incorporated with the ChG in such heterostructures typically sets a limitation; for example, the high material loss of silica glass and PMMA at long wavelengths is a drawback in MIR applications. The second strategy makes use of dispersion-engineered photonic crystal fibers (PCFs) [11,29,30] and suspended-core fibers [31–34], but these technologies have not yet reached the level of maturity of their silica-PCF counterparts. A third strategy utilizes bare ChG fiber tapers for dispersion engineering through an appropriate tapering ratio, while ensuring broadband single-mode guidance to produce SCG with a high-quality spatial profile [35,36]. Indeed, As_2Se_3 tapers with a

1.2 μm waist diameter demonstrated an enhanced nonlinearity of 62,000 times that of a standard silica single-mode fiber [35] (see also Refs. [36–39]). While silica tapers have long been a source for SCG [40], bare ChG tapers are extremely difficult to handle due to the inferior *mechanical* properties of ChGs compared to silica, which limits the utility of this approach despite its promise [36,41,42].

Recently, we developed a new extrusion-based technique for fabricating hybrid ChG/polymer fiber preforms that enable drawing extended lengths of *robust* ChG fibers that incorporate a thick built-in protective thermoplastic polymer jacket that is integral to the fiber structure [43]. This fabrication strategy resolves the traditional concerns of the mechanical fragility of ChGs without compromising their optical performance. In a hybrid fiber produced using this process, the optical properties are dictated by the ChG index-guiding structure, while the mechanical robustness derives from a millimeter-diameter built-in polymer jacket. In contrast to most alternative approaches, this process offers flexibility in choosing the geometric parameters (such as the core and cladding diameters) and gives access to a wide range of core and cladding ChG combinations and, thereby, provides control over their index contrast. Uniquely, the thermal compatibility between the ChG and the polymer allows for fiber tapering *without* first removing the polymer jacket, resulting in robust tapers that are easily handled and manipulated. Concomitantly, using ChGs jointly with a high core-to-cladding index contrast leads to strong confinement of the optical mode to the taper core [43], thereby enhancing the nonlinearity and enabling control over GVD. Furthermore, these nanotapers obviate the need for *in situ* tapering of ChG fibers [41,42] and the complications associated with precarious handling of traditional bare ChG tapers. We have recently reported the first observations of octave-spanning infrared SCG in such robust all-solid nanotapers with strong field confinement [44] and have provided a detailed investigation of their linear properties and GVD characteristics [21].

In this paper we present a systematic characterization of the *nonlinear* properties of robust, composite (multimaterial) ChG nanotapers produced using this novel fabrication methodology, which complements our recent study of their *linear* properties [21,43]. Using the standard Z-scan technique with femtosecond pulses, we measure the nonlinear index of refraction n_2 at a wavelength of $\lambda = 1.55$ μm in the bulk glasses that are incorporated in our fibers and, thence, the nanotapers. We next estimate n_2 in the nanotapers via self-phase modulation (SPM) measurements at low peak powers in both the picosecond- and femtosecond-pulse regimes. The values of n_2 estimated in bulk ChGs and those obtained in the nanotapers are in good agreement. These measurements provide the parameter values incorporated in a computational model we constructed for SCG in such nanotapers at higher peak powers. The predictions of this model are compared to SCG measurements using femtosecond pulses coupled to the nanotapers. The theoretical predictions and SCG measurements are in excellent agreement, thereby confirming the consistency and utility of our computational model. Our results clearly indicate the promise of robust composite ChG nanotapers produced using the multimaterial coextrusion approach as a viable technology to harness the unique capabilities of ChGs while circumventing some of their limitations.

Table 1. Linear Characterization of Bulk ChGs Used in Fiber Fabrication[a]

Glass	$\Delta\lambda$ (μm)	n	β_2 (ps^2/km)
As_2S_3	0.6–12.5	2.472 ± 0.015	978 ± 50
$As_2Se_{1.5}S_{1.5}$	0.75–13.5	2.743 ± 0.015	670 ± 50
As_2Se_3	0.85–18.5	2.904 ± 0.015	474 ± 50

[a]The transparency window $\Delta\lambda$ was determined by Fourier transform infrared spectroscopy (FTIR) transmission, while n and β_2 were obtained by spectral interferometry at $\lambda = 1.55$ μm [21].

2. NONLINEAR CHARACTERIZATION OF BULK CHALCOGENIDES

We start by characterizing the nonlinear characteristics of the ChGs of interest in bulk form. The ChGs used in fabricating the fibers and nanotapers investigated here were prepared from commercial glass (Amorphous Materials, Inc.) [43]. We produced 1-cm-diameter disk-shaped samples of three glasses: $As_2Se_{1.5}S_{1.5}$, As_2Se_3, and As_2S. 1.5-mm-thick samples were used to measure the spectral transmittance and nonlinear refractive index n_2, while 2.5-cm-long cylindrical rods were used to measure the GVD parameter β_2 and the linear refractive index n (at $\lambda = 1.55$ μm). The sample facets were all polished to submicrometer surface roughness. Table 1 summarizes the measured linear characteristics (see also Refs. [21,43]).

The nonlinear refractive indices n_2 of the ChGs were measured at $\lambda = 1.55$ μm by the standard Z-scan technique [45] using ~100 fs (FWHM) pulses generated by an optical parametric generator/amplifier (OPA/OPG, TOPAS-C Light Conversion Ltd.); see Appendix A for details. The closed- and open-aperture Z-scan data (along with fitted curves) are shown in Figs. 1(a) and 1(b), respectively, for the $As_2Se_{1.5}S_{1.5}$ sample.

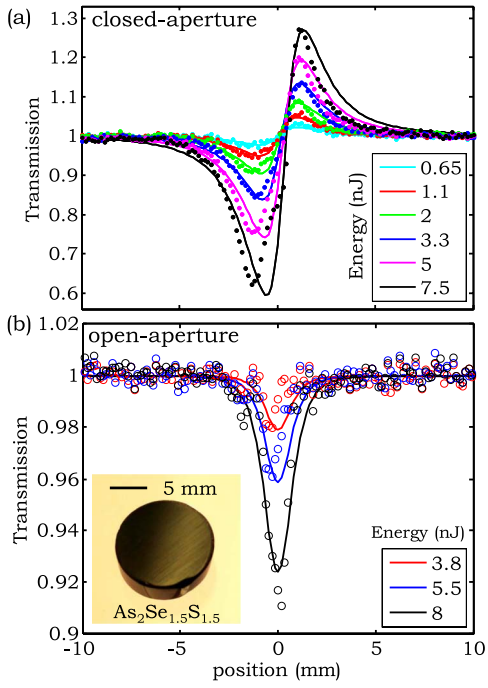

Fig. 1. (a) Closed-aperture and (b) open-aperture (*three*-photon absorption here) Z-scan results for a $As_2Se_{1.5}S_{1.5}$ sample at different incident femtosecond-pulse energies (see text and Appendix A for details). The dots are the measured values and the solid lines are the fitted curves. The inset in (b) is a photograph of the $As_2Se_{1.5}S_{1.5}$ sample.

After fitting the data, n_2 was found for As_2Se_3 to be $(5.2 \pm 1.0) \times 10^{-14}$ cm^2/W, for $As_2Se_{1.5}S_{1.5}$ to be $(4.6 \pm 0.9) \times 10^{-14}$ cm^2/W, and for As_2S_3 to be $(1.6 \pm 0.9) \times 10^{-14}$ cm^2/W. We note that the measurements for the $As_2Se_{1.5}S_{1.5}$ sample indicate *three*-photon absorption (3PA) in the open-aperture signal with a 3PA coefficient of $(5.5 \pm 2.5) \times 10^{-2}$ cm^3/GW^2 [Fig. 1(b)]. This measurement is consistent with the result $\approx 8.7 \times 10^{-2}$ cm^3/GW^2 calculated from a two-parabolic-band model (a more complete analysis is provided in [46]) assuming the bandgap is ≈1.74 eV, which is based on the linear transmittance spectrum of this ChG composition [21]. For the other two samples, no nonlinear absorption was observed for the irradiances used and *two*-photon absorption is not expected at this wavelength.

3. NONLINEAR CHARACTERIZATION OF ROBUST COMPOSITE CHG NANOTAPERS

A. Nanotaper Samples

We next investigate the nonlinear characteristics of robust composite ChG nanotapers produced using the novel fabrication approach described above. Our approaches to fiber preform fabrication, fiber drawing, and fiber tapering, in addition to linear optical and mechanical characterization of these unique fibers and nanotapers, have been reported elsewhere; see Refs. [21,43,44,47]. The step-index fiber we investigate here consists of a 10-μm-diameter $As_2Se_{1.5}S_{1.5}$ core and a 35-μm-diameter As_2S_3 cladding surrounded by a thick built-in 1.2-mm-diameter thermoplastic polymer jacket (polyethersulfone, PES) that does not participate in the optical functionality of the fiber, but dictates its superior mechanical robustness compared to a conventional all-ChG fiber [Figs. 2(a) and 2(b)] [43].

Nanotapers are produced using a home-built tapering setup [48]. Since the polymer (PES) is thermally compatible with the ChGs, the composite fiber may be tapered *without* removing the polymer jacket. The axial profile of the tapers can be controlled by adjusting the tapering speed, length, and temperature [21]. Utilizing this methodology, we have produced tapers with minimum core diameters at the taper axial midpoint d_c^{min} ranging from a few micrometers to <100 nm, and lengths ranging from a few millimeters to tens of centimeters (while avoiding potential fluid-instability-driven breakup mechanisms [48,49]).

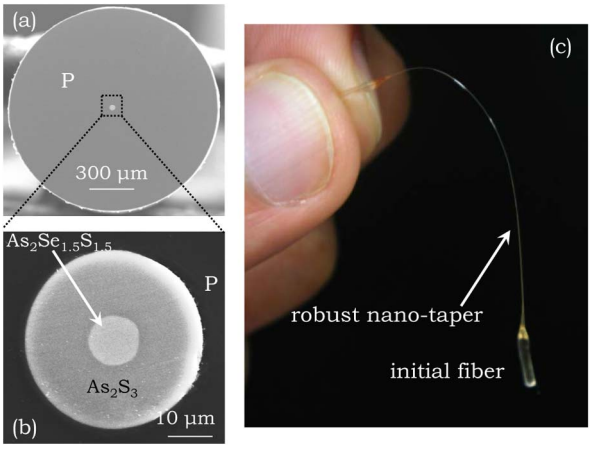

Fig. 2. (a) Scanning electron microscope (SEM) micrograph of the cross section of the robust, composite ChG fiber used to prepare the nanotaper samples. P: PES polymer jacket. (b) A higher-magnification SEM micrograph of the fiber cross section highlighting the ChG core/cladding structure. (c) A typical robust nanotaper with minimum core diameter at the axial midpoint of $d_c^{min} = 500$ nm maintained over ≈20% of its 50-mm length.

The robustness of the nanotapers is highlighted in Fig. 2(c), where we show a typical nanotaper produced in this fashion having $d_c^{min} = 500$ nm extending over 10 mm out of its 50-mm length, demonstrating the remarkable robustness of these hybrid-fiber nanowaveguide devices. Consequently, such nanotapers can be easily handled and manipulated. We typically fix the nanotaper to a glass slide using epoxy and then polish its end facets in preparation for the optical experiments [44]. Our previous investigations have confirmed that the relative sizes of the transverse features in these composite fibers are maintained in the tapering process [21,44,50], so we take the outer diameter to be in fixed relation to the core diameter d_c.

We plot the measured longitudinal profiles of the four nanotaper samples used in our measurements in Fig. 3(a). Other relevant parameters of the nanotaper Samples 1 through 4, such as the total length L, the minimum core diameter at the nanotaper axial midpoint d_c^{min}, and the optical transmission using CW laser light at $\lambda = 1.55$ μm (raw transmission, which includes ≈21.6% Fresnel reflection at each facet) are listed in Table 2. Although the short transition regions in the samples between the tapered and nontapered sections increase the optical losses, they nevertheless reduce the energy transfer from the cladding modes back into the core modes at the end of the tapered sections [51].

To set the stage for our nonlinear optical characterization experiments, we plot two optical parameters that change with core diameter d_c, and thus vary axially along the nanotaper: total GVD at $\lambda = 1.55$ μm and 2 μm [Fig. 3(b)], and the nonlinear parameter $\gamma = (2\pi n_2/\lambda A_{eff})$ [52] at $\lambda = 1.55$ μm [Fig. 3(c)]; here A_{eff} is the effective core area (see Ref. [52]). The total GVD is the sum of the measured material GVD and the calculated waveguide GVD [21]. Note that the GVD changes rapidly with d_c at the nanoscale due to strong field confinement effects (resulting from the large core/cladding index contrast) [21]. We plot β_2 also at $\lambda = 2$ μm to highlight the change in β_2 with wavelength and also in light of the current availability of high-power Tm-doped fiber lasers [53–56], which are potentially useful as pumps for SCG.

The diameter of the fundamental mode d_m (full width at $1/e^2$ from maximum) and the nonlinear coefficient γ are plotted in Fig. 3(c) as a function of d_c at $\lambda = 1.55$ μm. It is clear that three distinct regimes emerge in the dependence of γ on d_c. For large d_c (>3 μm), the fundamental mode is well confined to the core (>99%) due to the large core/cladding index contrast. In this regime, d_m and d_c are linearly related (with $d_m < d_c$). As d_c decreases, a concomitant reduction in the mode diameter d_m ensues, and consequently γ increases. This linear trend changes with further reduction in d_c, and at $d_c \sim 600$ nm the ratio d_m/d_c exceeds 1. At this point, the mode extends significantly out of the core and γ therefore decreases with reduction in d_c [Fig. 3(c), inset]. Finally, when $d_c < 450$ nm, the mode extends further into the ChG cladding and reaches the polymer jacket. Due to the large index contrast between the cladding ($n = 2.472$ for As_2S_3 at $\lambda = 1.55$ μm) and polymer ($n_{PES} = 1.61$ at $\lambda = 1.55$ μm), the mode remains confined in the cladding and γ increases again with further reduction in fiber diameter. Although γ continues

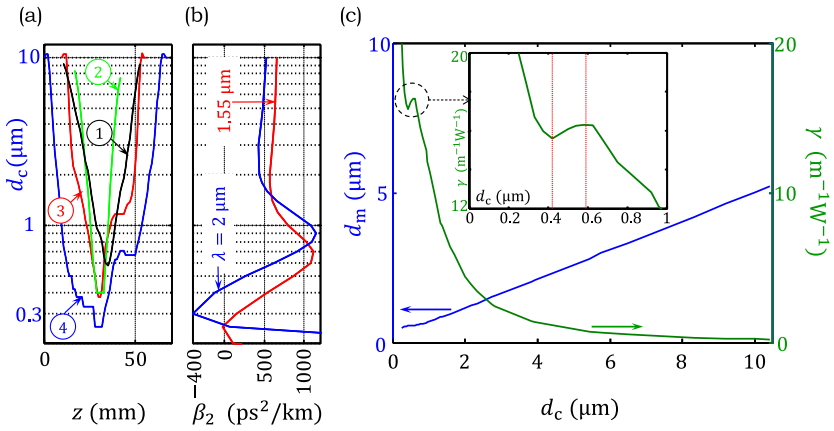

Fig. 3. (a) Longitudinal core diameter d_c profiles of the four samples used in the experiments; z is taken along the nanotaper axis. (d_c^{min}, L) of Samples through 4 are: (580 nm, 42 mm), (400 nm, 25 mm), (375 nm, 46 mm), and (250 nm, 68 mm), respectively. See also Table 2. (b) The total GVD parameter β_2 as a function d_c calculated at $\lambda = 1.55$ and 2 μm. (c) The blue curve (left vertical axis) shows the diameter of the fundamental mode d_m at $\lambda = 1.55$ μm, which indicates the optical-mode confinement when compared to d_c, and the green curve (right vertical axis) is the nonlinear coefficient γ of the fiber as a function of core diameter d_c, calculated for the fundamental mode at $\lambda = 1.55$ μm. The inset shows the region of the curve of γ that is encircled (dashed circle) and highlights the non-monotonic relationship between d_m and d_c at submicrometer core diameters (250 nm < d_c < 1 μm). The two-dashed vertical lines in the inset correspond to $d_c = 600$ nm (where d_m/d_c exceeds 1) and $d_c = 450$ nm (where confinement by the polymer jacket starts to dominate). See text for details.

to increase by reducing d_c, the high infrared optical losses in the polymer [21] obviates the advantages accrued by further tapering. Hence, from these considerations we conclude that, for SCG applications using these hybrid nanotapers, the optimum d_c^{min} value is several hundreds of nanometers, while L should not exceed a few centimeters to avoid heavy infrared losses in the polymer jacket (which may be reduced by increasing the diameter of the ChG cladding). The nanotaper samples investigated here were prepared in accordance with these guidelines to confirm the design principles.

B. Nonlinear Characterization Methodology

We now proceed to describe the results of the nonlinear characterization experiments carried out on our nanotapers. Two classes of experiments were performed. In the first, we obtained an independent measurement of n_2 from observations of spectral broadening resulting from SPM using low-peak-power picosecond and femtosecond laser pulses. In the second class of experiments, we used higher peak-power femtosecond pulses to observe SCG extending over one octave of bandwidth. We then employed a computational model that utilizes parameters extracted from our linear and nonlinear measurements to validate the spectral broadening observed.

Both classes of experiments (SPM and SCG) were carried out using the setup shown in Fig 4. We used fiber-coupled lasers at $\lambda = 1.55$ μm and the collimated beam was coupled in and then out of the 10-μm-diameter core of the nontapered ends of the nanotaper samples [Fig. 2] using a pair of aspheric lenses having 6.2-mm focal length. An infrared camera (7290A MicronViewer) was used to monitor the beam profile and optimize the coupling into the core. The output spectrum was measured with 0.1-nm spectral resolution using two optical spectrum analyzers (OSAs) to cover the 1–2 μm spectral range: Advantest Q8381A (up to $\lambda = 1.7$ μm) and Yokogawa AQ6375 (beyond $\lambda = 1.7$ μm). Two laser sources at $\lambda = 1.55$ μm were used. The first is a femtosecond passively mode-locked fiber laser (Calmar, FPL-M2CFF) producing pulses with a 400-fs FWHM pulsewidth at a 20-MHz repetition rate and a 1.7-mW average power (corresponding to a maximum peak power of 212 W). The second is a passively mode-locked erbium-doped fiber laser (PriTel, PFL-10000) producing picosecond pulses with a 10-ps FWHM pulses at 5 MHz repetition rate and 4.5 mW average power (corresponding to a maximum peak power of 90 W).

Table 2. Nanotaper Sample Parameters[a]

Sample	1	2	3	4
d_c^{min} (in nm)	580	400	375	250
L (in mm)	42	25	46	68
T (%) at $\lambda = 1.55$ μm	35	32	28	26

[a]Here d_c^{min} is the minimum core diameter at the nanotaper axial midpoint; L is the nanotaper total length; T is the sample transmission (including the Fresnel reflection at the facets).

C. Self-Phase Modulation Measurements

The goal of this experiment is to estimate n_2 of the ChGs in the nanotaper form-factor and to confirm and complement the values obtained in bulk ChG using Z-scan measurements. We extract n_2 from the total nonlinear phase shift [52] of an optical pulse traversing the nanotapers as estimated from the spectral broadening.

First, coupling at the input 4.5 mW average-power picosecond pulses (90 W peak power) to nanotaper Sample 4 [Fig. 5(a)] and 1.7 mW average-power femtosecond pulses (212 W peak-power) to nanotaper Sample 2 [Fig. 5(b)] both led to the development of three distinct spectral peaks. Varying the input power using a variable attenuator leads to a gradual evolution of the output spectrum from the single-peaked input to the three-peaked output spectra shown in Fig. 5.

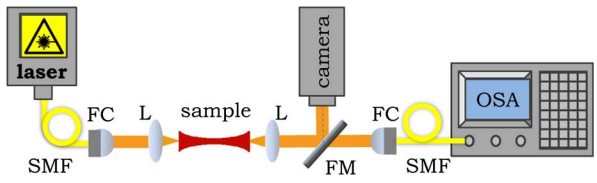

Fig. 4. Experimental setup for SPM and SCG characterization. L, aspheric lens; FC, fiber collimator; FM, flip mirror; SMF, single-mode fiber. Two identical lenses L are used at the nanotaper sample input and output for coupling.

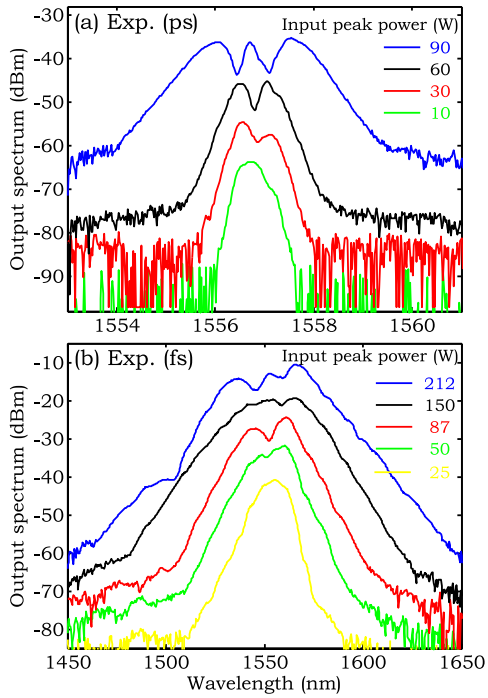

Fig. 5. SPM characterization results obtained in two different experiments: (a) picosecond pulses launched into nanotaper Sample 4 and (b) femtosecond pulses launched into nanotaper Sample 2. The power levels are the input peak powers for each sample without corrections for Fresnel reflection from the sample facets.

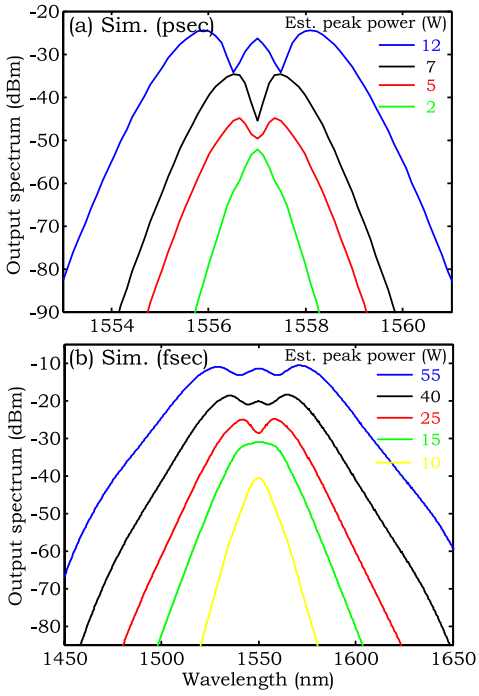

Fig. 6. SPM simulation results for the two different experiments shown in Fig. 5: (a) picosecond pulses launched into Sample 4 and (b) femtosecond pulses launched into Sample 2. The power levels are the estimated peak powers in the tapered section of each sample after correcting for Fresnel reflections at the sample facets and nanotaper losses (see text for details).

To extract an estimate of n_2 from these spectral broadening experiments we compared the spectra with simulated spectra obtained by solving the generalized nonlinear Schrödinger equation (GNLSE) using the symmetrized split-step method [52] taking into account the axial variation in the optical mode, GVD, and γ as given in Fig. 3; see Appendix B for details. In estimating the power coupled into the fundamental mode at the nanotaper waist, where most of the nonlinear phase accumulates, several factors must be accounted for: input coupling efficiency, Fresnel reflection at the facets, linear fiber loss, tapering loss, scattering, and potentially nonlinear absorption. The measured input and output power levels after accounting for Fresnel reflection-place upper and lower bounds on the power at the nanotaper waist. For each input power level, we carried out the simulations while scanning the resultant power at the nanotaper waist between these two bounds and also the values for n_2 to optimize the matching between the measured and simulated spectra. The simulated spectra thus obtained are in good agreement with the experimental results in both the picosecond and femtosecond pulse regimes [Figs. 6(a) and 6(b)]. The n_2 values obtained from the picosecond and femtosecond SPM measurements are $(3.75 \pm 1.45) \times 10^{-14}$ cm^2/W and $(3.15 \pm 0.85) \times 10^{-14}$ cm^2/W, respectively. The values are slightly lower than the n_2 value obtained in bulk $As_2Se_{1.5}S_{1.5}$ given above that was measured via the Z-scan technique. This result is expected since the n_2 values obtained from the nanotapers combine the impact of both the core and the cladding ChGs (the cladding has lower n_2 than the core).

D. Supercontinuum Generation Measurements

Experiments were performed to demonstrate the potential of such robust multimaterial nanotapers for efficient SCG using femtosecond pulses. At relatively low power levels (peak power ~100 W, corresponding to 40 pJ of energy per pulse), we achieve hundreds of nanometers of spectral broadening in these nanotapers [Fig. 7(a)]. Moreover, the agreement

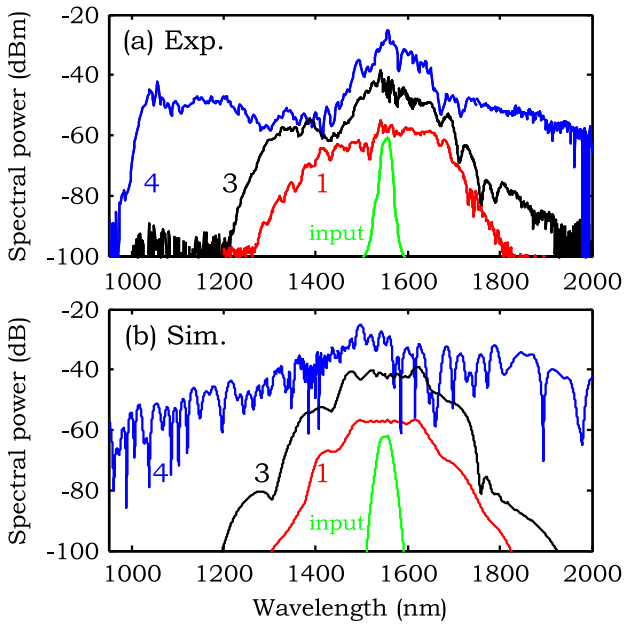

Fig. 7. (a) Measured and (b) simulated supercontinua for Sample 1, Sample 3, and Sample 4 when femtosecond pulses are launched. The input pulse parameters are as follows: 4.5 mW average power, 20 MHz repetition rate, and 400 fs FWHM pulsewidth. The peak power levels in the simulated spectra are estimated at 125, 100, and 106 W for Sample 1, Sample 3, and Sample 4, respectively.

between the measured supercontinua and their simulated counterparts [Fig. 7(b)] that were obtained using the measured sample parameters further confirm the validity and consistency of our computational model [Appendix B].

The femtosecond laser was coupled to Sample 1, Sample 3, and Sample 4; the measured output spectra are shown in Fig. 7(a). The supercontinuum produced by Sample 1 spans 1.3–1.75 μm, while that produced by Sample 3 was slightly broader to cover 1.2–1.9 μm, which we attribute mainly to its lower GVD compared to Sample 1 [see Figs. 3(a) and 3(b)]. The broadest spectrum was achieved by Sample 4, which has the longest tapered section and the smallest $d_c^{\min}$, resulting in one octave of supercontinuum bandwidth, 1–2 μm. Some slow variations in power and drift occurring over time scales of the order of a few minutes were observed in the spectra during the measurements. We hypothesize that these fluctuations originate from a combination of thermal effects and multimodal interactions in the samples. In each case, after adjusting the input lens to slightly modify the coupling, the spectrum was immediately retrieved. We expect that further optimization of the nanotaper profiles will lead to enhanced spectral stability.

We finally note a surprising result that we have not yet accounted for. It is expected in the normal GVD regime and confirmed by our simulations that SPM dominates over four-wave mixing and Raman scattering mechanisms in producing spectral broadening. Nevertheless, at power levels higher than those reported in Fig. 7, we achieve supercontinua with bandwidths that substantially exceed those predicted by our simulations. We have found that this broader spectrum cannot be attributed to an underestimation of n_2 or input coupled power levels. A computational search in the physical parameter space reveals that the most likely hypothesis is that the nanotaper GVD has undergone a large reduction (by ≈50%). This assumption allows us to reproduce the observed spectra observed at elevated power levels. At this point, we hypothesize that the high optical intensity in the nanotaper waist may lead to an increase in the local temperature, which in turn either alters the material GVD [57] or changes d_c along the nanotaper. While the estimation of γ is robust against perturbations in d_c [Fig. 3(b)], waveguide GVD undergoes large changes with small variations in d_c due to the strong field confinement in this high-index-contrast structure [21], which may explain our observations. We will pursue these observations further in future investigations.

4. CONCLUSION

In conclusion, we have presented the results of nonlinear characterization of ChG bulk samples (via the Z-scan technique) and of robust composite ChG nanotapers (via spectral broadening resulting from SPM). These nanotapers were prepared from step-index ChG fibers produced from the bulk ChGs we investigated. The fibers have a unique structure that makes them particularly apt for nonlinear MIR applications. Specifically, a thick built-in polymer jacket is provided to the ChG core/cladding, which vastly improves the fiber mechanical properties over conventional bare ChG fibers. The thermal compatibility of the polymer and the ChGs allowed us to prepare robust nanotapers without removing the polymer. Using picosecond and femtosecond pulses at $\lambda = 1.55$ μm launched into the nanotaper samples, we find good agreement between the nonlinear refractive index estimated from SPM observations and those estimated from Z-scan measurements of the bulk ChGs. The large core-to-cladding index contrast leads to strong mode confinement, enhances the optical nonlinearities in the nanotapers, and enables dispersion engineering leading to a full octave 1–2 μm SCG using low-peak-power femtosecond pulses. The results were compared to a computational model that makes use of optical parameters extracted from the samples, and good agreement between the measurements and the simulations was obtained. Our results indicate that such novel robust, multimaterial ChG nanotapers offer a useful platform for MIR SCG and infrared nonlinear fiber optics in general.

APPENDIX A: Z-SCAN MEASUREMENT

The nonlinear refractive indices n_2 of the ChGs we make use of here were measured at $\lambda = 1.55$ μm by the Z-scan technique [45] using ≈100 fs (FWHM) pulses generated by an OPA/OPG (Light Conversion Ltd. model TOPAS-C) pumped by a regenerative Ti:sapphire amplifier (Clark-MXR CPA-2010) operating at a 1 kHz repetition rate, delivering ≈1 mJ pulses at 780 nm. To verify the setup accuracy and calibrate the input-beam spot size and pulse duration, open-aperture Z-scans were performed on the bulk semiconductor GaAs [58], for which the two-photon absorption spectrum is theoretically calculated and experimentally verified (14 cm/GW) [59]. Closed-aperture Z-scan measurements are also calibrated against fused silica with documented n_2 values ($n_2^{\text{quartz}} = 2.6 \times 10^{-16}$ cm^2/W) [60]. Due to sample inhomogeneity, surface irregularities, or nonparallel facets, a linear transmittance change of ~20% was observed using a small spot size and weak probe beam scanning across the sample; therefore, initial Z-scan traces showed a large background. To obtain the Z-scan background, a low-energy Z-scan (0.3–0.5 nJ) was performed, restricted by the sensitivity of the Ge detectors, prior to higher energy Z-scans. All Z-scan curves at higher energy levels are then obtained by dividing the normalized raw data with this low-energy scan to cancel the background. Due to relatively large n_2 values of the samples, a small closed-aperture signal, estimated to be about 4%–5% from peak to valley, was already induced but buried in the background signal. Given the fact that only n_2 and no higher order nonlinearity is involved in nonlinear refraction, the energy of the "background-free" Z-scan curves [shown in Fig. 1(a)] is estimated by subtracting the actual energy from the background scan energy.

APPENDIX B: SIMULATIONS

Simulations of the nonlinear propagation dynamics of ultrafast pulses along nanotapers with axially varying diameter were carried out using the generalized nonlinear Schrödinger equation (GNLSE) [24] integrated via the symmetrized split-step method [52]. In our simulations, we included in the GNLSE terms that account for the following effects: (1) wavelength-dependent linear loss, (2) GVD, (3) SPM, (4) Raman response, and (5) self-steepening. Some of these effects depend on the core diameter d_c and, hence, vary along the nanotaper axis z. A linearly polarized transform-limited Gaussian pulse (discretized on a lattice of 2^{15} points) is launched in the fundamental mode. To ensure convergence we adaptively changed the axial step size to restrict the nonlinear SPM phase

shift to 0.001 rad/step [44]. The parameters used in the simulations were chosen as follows.

(1) Linear spectral losses were determined by FTIR transmission measurements [21].

(2) The GVD used was the sum of the material GVD for the core ChG (measured in bulk [21]) and the waveguide GVD calculated in COMSOL using the refractive indices in Table 1 and the axial profiles of the nanotaper samples shown in Fig. 3(a). We assumed that the material GVD varied linearly between $\lambda = 1.55$ and 2 μm; higher-order dispersion terms were neglected.

(3) The SPM term depends on mode confinement (related to d_c and the core-to-cladding index contrast) and the nonlinear indices n_2 for the core and cladding ChGs. We calculated the axially varying fundamental mode field distribution along the nanotaper using COMSOL (at $\lambda = 1.55$ μm) and used the bulk n_2 values reported above. At the input, $\gamma = 0.23$ W^{-1} m^{-1} where $d_c = 10$ μm, which subsequently increases to $\gamma = 4.41$, 11.72, and 19.95 W^{-1} m^{-1} at $d_c = 2$ μm, 1 μm, and 250 nm, respectively.

(4) The Raman response function and Raman strength coefficient for $As_2Se_{1.5}S_{1.5}$ are taken to be an average of those for As_2Se_3 [61] and As_2S_3 [62].

(5) The self-steepening is modeled to first order using an optical-shock time constant $\tau_s = (1/\omega_o)$ [24], where ω_o is the optical frequency corresponding to the central wavelength.

The integration of the parametric four-wave-mixing gain over the length of nanotapers was found not to play a significant role in the spectral broadening, so four-wave mixing was neglected in our calculations.

ACKNOWLEDGMENTS

We thank J. J. Kaufman, O. M. Piracha, D. Nguyen, L. Shah, and M. C. Richardson for assistance and loan of equipment. We are particularly grateful to E. W. Van Stryland and D. J. Hagan for granting us access to their laboratory and to the Z-scan measurement setup, and for valuable comments on the manuscript. This work was supported by the U.S. National Science Foundation (ECCS-1002295).

REFERENCES

1. J. S. Sanghera, I. D. Aggarwal, L. B. Shaw, L. E. Busse, P. Thielen, V. Nguyen, P. Pureza, S. Bayya, and F. Kung, "Applications of chalcogenide glass optical fibers at NRL," J. Optoelectron. Adv. Mater. **3**, 627–640 (2001).
2. B. J. Eggleton, B. Luther-Davies, and K. Richardson, "Chalcogenide photonics," Nat. Photonics **5**, 141–148 (2011).
3. A. Zakery and S. R. Elliott, *Optical Nonlinearities in Chalcogenide Glasses and their Applications* (Springer-Verlag, 2007).
4. M. Asobe, "Nonlinear optical properties of chalcogenide glass fibers and their application to all-optical switching," Opt. Fiber Technol. **3**, 142–148 (1997).
5. G. Lenz, J. Zimmermann, T. Katsufuji, M. E. Lines, H. Y. Hwang, S. Spälter, R. E. Slusher, S.-W. Cheong, J. S. Sanghera, and I. D. Aggarwal, "Large Kerr effect in bulk Se-based chalcogenide glasses," Opt. Lett. **25**, 254–256 (2000).
6. Q. Liu, X. Zhao, F. Gan, J. Mi, and S. Qian, "Femtosecond optical Kerr effect study of amorphous chalcogenide films," J. Non-Cryst. Solids **352**, 2351–2354 (2006).
7. L. Fu, V. G. Ta'eed, E. C. Mägi, I. C. M. Littler, M. D. Pelusi, M. R. E. Lamont, A. Fuerbach, H. C. Nguyen, D. I. Yeom, and B. J. Eggleton, "Highly nonlinear chalcogenide fibres for all-optical signal processing," Opt. Quantum Electron. **39**, 1115–1131 (2007).
8. Y. Xu, H. Zeng, G. Yang, G. Chen, Q. Zhang, and L. Xu, "Third-order nonlinearities in $GeSe_2In_2Se_3CsI$ glasses for telecommunications applications," Opt. Mater. **31**, 75–78 (2008).
9. M. D. Pelusi, F. Luan, E. Magi, M. R. Lamont, D. J. Moss, B. J. Eggleton, J. S. Sanghera, L. B. Shaw, and I. D. Aggarwal, "High bit rate all-optical signal processing in a fiber photonic wire," Opt. Express **16**, 11506–11512 (2008).
10. B. J. Eggleton, T. D. Vo, R. Pant, J. Schröder, M. D. Pelusi, D. Y. Choi, S. J. Madden, and B. L. Davies, "Photonic chip based ultrafast optical processing based on high nonlinearity dispersion engineered chalcogenide waveguides," Laser Photon. Rev. **6**, 97–114 (2012).
11. L. B. Shaw, P. A. Thielen, F. H. Kung, V. Q. Nguyen, J. Sanghera, and I. Aggarwal, "IR supercontinuum generation in As–Se photonic crystal fiber," in *Proceedings of Advanced Solid State Photonics* (2005), paper TuC5.
12. R. R. Gattass, L. B. Shaw, V. Nguyen, P. Pureza, I. D. Aggarwal, and J. S. Sanghera, "All-fiber chalcogenide-based mid-infrared supercontinuum source," Opt. Fiber Technol. **18**, 345–348 (2012).
13. P. Domachuk, N. A. Wolchover, M. Cronin-Golomb, A. Wang, A. K. George, C. M. B. Cordeiro, J. C. Knight, and F. G. Omenetto, "Over 4000 nm bandwidth of mid-IR supercontinuum generation in sub-centimeter segments of highly nonlinear tellurite PCFs," Opt. Express **16**, 7161–7168 (2008).
14. G. Qin, X. Yan, C. Kito, M. Liao, T. Suzuki, A. Mori, and Y. Ohishi, "Highly nonlinear tellurite microstructured fibers for broadband wavelength conversion and flattened supercontinuum generation," J. Appl. Phys. **107**, 043108 (2010).
15. Z. Chen, A. J. Taylor, and A. Efimov, "Coherent mid-infrared broadband continuum generation in non-uniform ZBLAN fiber taper," Opt. Express **17**, 5852–5860 (2009).
16. O. P. Kulkarni, V. V. Alexander, M. Kumar, M. J. Freeman, M. N. Islam, F. L. Terry, Jr., M. Neelakandan, and A. Chan, "Supercontinuum generation from ~1.9 to 4.5 μm in ZBLAN fiber with high average power generation beyond 3.8 μm using a thulium-doped fiber amplifier," J. Opt. Soc. Am. B **28**, 2486–2498 (2011).
17. J. S. Sanghera, L. B. Shaw, and I. D. Aggarwal, "Applications of chalcogenide glass optical fibers," C.R. Chim. **5**, 873–883 (2002).
18. C. Florea, L. Busse, J. Sanghera, B. Shaw, and I. R. Aggarwal, "A simple phenomenological study of photodarkening in As_2S_3 glasses," Opt. Mater. **34**, 1389–1393 (2012).
19. I. V. Fekeshgazi, K. V. Mai, N. I. Matelesko, V. M. Mitsa, and E. I. Borkach, "Structural transformations and optical properties of As_2S_3 chalcogenide glasses," Semiconductors **39**, 951–954 (2005).
20. R. E. Slusher, G. Lenz, J. Hodelin, J. Sanghera, L. B. Shaw, and I. D. Aggarwal, "Large Raman gain and nonlinear phase shifts in high-purity As_2Se_3 chalcogenide fibers," J. Opt. Soc. Am. B **21**, 1146–1155 (2004).
21. S. Shabahang, G. Tao, J. J. Kaufman, and A. F. Abouraddy, "Dispersion characterization of chalcogenide bulk glass, composite fibers, and robust nanotapers," J. Opt. Soc. Am. B **30**, 2498–2506 (2013).
22. M. Duhant, W. Renard, G. Canat, T. N. Nguyen, F. Smektala, J. Troles, Q. Coulombier, P. Toupin, L. Brilland, P. Bourdon, and G. Renversez, "Fourth-order cascaded Raman shift in AsSe chalcogenide suspended-core fiber pumped at 2 μm," Opt. Lett. **36**, 2859–2861 (2011).
23. L. B. Shaw, R. R. Gattass, J. S. Sanghera, and I. D. Aggarwal, "All-fiber mid-IR supercontinuum source from 1.5 to 5 μm," Proc. SPIE **7914**, 79140P (2011).
24. J. M. Dudley, G. Genty, and S. Coen, "Supercontinuum generation in photonic crystal fiber," Rev. Mod. Phys. **78**, 1135–1184 (2006).
25. N. Granzow, S. Stark, M. Schmidt, A. Tverjanovich, A. L. Wondraczek, and P. Russell, "Supercontinuum generation in chalcogenide-silica step-index fibers," Opt. Express **19**, 21003–21010 (2011).
26. R. Ahmad and M. Rochette, "High efficiency and ultra broadband optical parametric four-wave mixing in chalcogenide-PMMA hybrid microwires," Opt. Express **20**, 9572–9580 (2012).
27. C. Baker and M. Rochette, "High nonlinearity and single-mode transmission in tapered multimode As_2Se_3-PMMA fibers," IEEE Photon. J. **4**, 960–969 (2012).

28. C. Chaudhari, M. Liao, T. Suzuki, and Y. Ohishi, "Chalcogenide core tellurite cladding composite microstructured fiber for nonlinear applications," J. Lightwave Technol. **30**, 2069–2076 (2012).
29. L. Brilland, F. Smektala, G. Renversez, T. Chartier, J. Troles, T. N. Nguyen, N. Traynor, and A. Monteville, "Fabrication of complex structures of holey fibers in chalcogenide glass," Opt. Express **14**, 1280–1285 (2006).
30. W. Gao, M. Liao, X. Yan, C. Kito, T. Kohoutek, T. Suzuki, M. E. Amraoui, J. C. Jules, G. Gadret, F. Désévédavy, F. Smektala, and Y. Ohishi, "Visible light generation and its influence on supercontinuum in chalcogenide As_2S_3 microstructured optical fiber," Appl. Phys. Express **4**, 102601 (2011).
31. M. El-Amraoui, G. Gadret, J. C. Jules, J. Fatome, C. Fortier, F. Désévédavy, I. Skripatchev, Y. Messaddeq, J. Troles, L. Brilland, W. Gao, T. Suzuki, Y. Ohishi, and F. Smektala, "Microstructured chalcogenide optical fibers from As_2S_3 glass: towards new IR broadband sources," Opt. Express **18**, 26655–26665 (2010).
32. K. M. Mohsin, M. S. Alam, D. M. N. Hasan, and M. N. Hossain, "Dispersion and nonlinearity properties of a chalcogenide As_2Se_3 suspended core fiber," Appl. Opt **50**, E102–E107 (2011).
33. M. El-Amraoui, J. Fatome, J. C. Jules, B. Kibler, G. Gadret, C. Fortier, F. Smektala, I. Skripatchev, C. Polacchini, Y. Messaddeq, J. Troles, L. Brilland, M. Szpulak, and G. Renversez, "Strong infrared spectral broadening in low-loss As-S chalcogenide suspended core microstructured optical fibers," Opt. Express **18**, 4547–4556 (2010).
34. M. Liao, X. Yan, G. Qin, C. Chaudhari, T. Suzuki, and Y. Ohishi, "Controlling the chromatic dispersion of soft glass highly nonlinear fiber through complex microstructure," J. Non-Cryst. Solids **356**, 2613–2617 (2010).
35. E. C. Mägi, L. B. Fu, H. C. Nguyen, M. R. E. Lamont, D. I. Yeom, and B. J. Eggleton, "Enhanced Kerr nonlinearity in subwavelength diameter As_2Se_3 chalcogenide fiber tapers," Opt. Express **15**, 10324–10329 (2007).
36. D. D. Hudson, S. A. Dekker, E. C. Mägi, A. C. Judge, S. D. Jackson, E. Li, J. S. Sanghera, L. B. Shaw, I. D. Aggarwal, and B. J. Eggleton, "Octave spanning supercontinuum in an As_2S_3 taper using ultralow pump pulse energy," Opt. Lett. **36**, 1122–1124 (2011).
37. L. B. Fu, M. D. Pelusi, E. C. Mägi, V. G. Ta'eed, and B. J. Eggleton, "Broadband all-optical wavelength conversion of 40 Gbit/s," Electron. Lett. **44**, 44–46 (2008).
38. D. I. Yeom, E. C. Mägi, M. R. E. Lamont, M. A. F. Roelens, L. Fu, and B. J. Eggleton, "Low-threshold supercontinuum generation in highly nonlinear chalcogenide nanowires," Opt. Lett. **33**, 660–662 (2008).
39. F. Luan, J. Van Erps, M. D. Pelusi, E. Mägi, T. Iredale, H. Thienpont, and B. J. Eggleton, "High-resolution optical sampling of 640 Gbit/s data using dispersion-engineered chalcogenide photonic wire," Electron. Lett. **46**, 231–232 (2010).
40. T. A. Birks, W. J. Wadsworth, and P. St. J. Russell, "Supercontinuum generation in tapered fibers," Opt. Lett. **25**, 1415–1417 (2000).
41. A. Marandi, C. W. Rudy, V. G. Plotnichenko, E. M. Dianov, K. L. Vodopyanov, and R. L. Byer, "Mid-infrared supercontinuum generation in tapered chalcogenide fiber for producing octave-spanning frequency comb around 3 μm," Opt. Express **20**, 24218–24225 (2012).
42. C. W. Rudy, A. Marandi, K. L. Vodopyanov, and R. L. Byer, "Octave-spanning supercontinuum generation in *in situ* tapered As_2S_3 fiber pumped by a thulium-doped fiber laser," Opt. Lett. **38**, 2865–2868 (2013).
43. G. Tao, S. Shabahang, E.-H. Banaei, J. J. Kaufman, and A. F. Abouraddy, "Multimaterial preform coextrusion for robust chalcogenide optical fibers and tapers," Opt. Lett. **37**, 2751–2753 (2012).
44. S. Shabahang, M. P. Marquez, G. Tao, M. U. Piracha, D. Nguyen, P. J. Delfyett, and A. F. Abouraddy, "Octave-spanning infrared supercontinuum generation in robust chalcogenide nanotapers using picosecond pulses," Opt. Lett. **37**, 4639–4641 (2012).
45. M. Sheik-Bahae, A. A. Said, T. H. Wei, D. J. Hagan, and E. W. Van Stryland, "Sensitive measurement of optical nonlinearities using a single beam," IEEE J. Quantum Electron. **26**, 760–769 (1990).
46. P. D. Olszak, C. M. Cirloganu, S. Webster, L. A. Padilha, T. R. Ensley, H. Hu, G. Nootz, D. J. Hagan, and E. W. Van Stryland, CREOL, Orlando, Florida, 32816 USA, are preparing a manuscript to be called "Three-photon absorption in direct-gap semiconductors."
47. G. Tao, A. M. Stolyarov, and A. F. Abouraddy, "Multimaterial fibers," Int. J. Appl. Glass Sci. **3**, 349–368 (2012).
48. S. Shabahang, J. J. Kaufman, D. S. Deng, and A. F. Abouraddy, "Observation of the Plateau–Rayleigh capillary instability in multi-material optical fibers," Appl. Phys. Lett. **99**, 161909 (2011).
49. J. J. Kaufman, G. Tao, S. Shabahang, E.-H. Banaei, D. S. Deng, X. Liang, S. G. Johnson, Y. Fink, and A. F. Abouraddy, "Structured spheres generated by an in-fibre fluid instability," Nature **487**, 463–467 (2012).
50. J. J. Kaufman, G. Tao, S. Shabahang, D. S. Deng, Y. Fink, and A. F. Abouraddy, "Thermal drawing of high-density macroscopic arrays of well-ordered sub-5-nm-diameter nanowires," Nano Lett. **11**, 4768–4773 (2011).
51. G. Brambilla, F. Xu, P. Horak, Y. Jung, F. Koizumi, N. P. Sessions, E. Koukharenko, X. Feng, G. S. Murugan, J. S. Wilkinson, and D. J. Richardson, "Optical fiber nanowires and microwires: fabrication and applications," Adv. Opt. Photon. **1**, 107–161 (2009).
52. G. P. Agrawal, *Nonlinear Fiber Optics* (Academic, 2001).
53. G. Imeshev and M. E. Fermann, "230-kW peak power femtosecond pulses from a high power tunable source based on amplification in Tm-doped fiber," Opt. Express **13**, 7424–7431 (2005).
54. M. A. Solodyankin, E. D. Obraztsova, A. S. Lobach, A. I. Chernov, A. V. Tausenev, V. I. Konov, and E. M. Dianov, "Mode-locked 1.93 μm thulium fiber laser with a carbon nanotube absorber," Opt. Lett. **33**, 1336–1338 (2008).
55. K. Kieu and F. W. Wise, "Soliton thulium-doped fiber laser with carbon nanotube saturable absorber," IEEE Photon. Technol. Lett. **21**, 128–130 (2009).
56. F. Haxsen, D. Wandt, U. Morgner, J. Neumann, and D. Kracht, "Pulse characteristics of a passively mode-locked thulium fiber laser with positive and negative cavity dispersion," Opt. Express **18**, 18981–18988 (2010).
57. M. Yaman, H. E. Kondakci, and M. Bayindir, "Large and dynamical tuning of a chalcogenide Fabry–Perot cavity mode by temperature modulation," Opt. Express **18**, 3168–3173 (2010).
58. W. C. Hurlbut, Y.-S. Lee, K. L. Vodopyanov, P. S. Kuo, and M. M. Fejer, "Multiphoton absorption and nonlinear refraction of GaAs in the mid-infrared," Opt. Lett. **32**, 668–670 (2007).
59. M. Sheik-Bahae, D. C. Hutchings, D. J. Hagan, and E. W. Van Stryland, "Dispersion of bound electronic nonlinear refraction in solids," IEEE J. Quantum Electron. **27**, 1296–1309 (1991).
60. D. Milam, "Review and assessment of measured values of the nonlinear refractive-index coefficient of fused silica," Appl. Opt. **37**, 546–550 (1998).
61. J. Hu, C. R. Menyuk, L. B. Shaw, J. S. Sanghera, and I. D. Aggarwal, "Maximizing the bandwidth of supercontinuum generation in As_2Se_3 chalcogenide fibers," Opt. Express **18**, 6722–6739 (2010).
62. C. Xiong, E. Magi, F. Luan, A. Tuniz, S. Dekker, J. S. Sanghera, L. B. Shaw, I. D. Aggarwal, and B. J. Eggleton, "Characterization of picosecond pulse nonlinear propagation in chalcogenide As_2S_3 fiber," Appl. Opt. **48**, 5467–5474 (2009).